

SECOND-ORDER FULLY DISCRETE CENTRAL-UPWIND SCHEME FOR TWO-DIMENSIONAL HYPERBOLIC SYSTEMS OF CONSERVATION LAWS*

ALEXANDER KURGANOV[†], MARTINA PRUGGER[‡], AND TONG WU[§]

Abstract. In this paper, we derive a new second-order fully discrete Godunov-type central-upwind scheme for two-dimensional hyperbolic systems of conservation laws. The scheme is derived in three steps: reconstruction, evolution, and projection. The novelty of our approach is in the evolution step, which is performed using the nonuniform quadrilateral control volumes obtained based on the one-sided local speeds of propagation, and in the projection step, in which the evolved solution is projected back onto the uniform grid with the help of a new sharp piecewise polynomial reconstruction. The scheme is tested on a number of numerical examples for the Euler equations of gas dynamics. We have demonstrated that the new scheme is nonoscillatory and at the same time it achieves higher resolution than the second-order semidiscrete central-upwind scheme. The latter suggests that the fully discrete scheme has a smaller amount of numerical dissipation.

Key words. two-dimensional hyperbolic systems of conservation laws, Godunov-type finite-volume schemes, central-upwind schemes, Euler equations of gas dynamics

AMS subject classifications. 76M12, 65M08, 35L65

DOI. 10.1137/15M1038670

1. Introduction. We consider hyperbolic systems of conservation laws, which in the two-dimensional (2-D) case can be written as

$$(1.1) \quad \mathbf{U}_t + \mathbf{F}(\mathbf{U})_x + \mathbf{G}(\mathbf{U})_y = \mathbf{0}.$$

Here, $\mathbf{U}(x, y, t) = (u_1(x, y, t), \dots, u_N(x, y, t))^T$ is an N -dimensional vector of conserved quantities that depends on the time variable t and the two spatial variables x and y , and \mathbf{F} and \mathbf{G} are nonlinear fluxes in the x - and y -directions, respectively.

Development of accurate and robust numerical methods for general 2-D systems (1.1) is a challenging task since their solutions typically develop nonsmooth structures containing shock waves, rarefaction waves, and contact waves propagating in a variety of directions and interacting in a complicated way, which is yet to be fully understood even for the widely studied compressible Euler equations; see, e.g., [3, 23, 37, 38]. Most of the upwind Godunov-type finite-volume methods are based on the “dimension-by-dimension” approach so that the numerical fluxes through the boundaries of the finite-volume cells are computed by (approximately) solving a one-dimensional (1-D) generalized Riemann problem in the normal direction; see, e.g., [2, 6, 11, 20, 34]. There

*Submitted to the journal’s Methods and Algorithms for Scientific Computing section September 8, 2015; accepted for publication (in revised form) January 17, 2017; published electronically May 25, 2017.

<http://www.siam.org/journals/sisc/39-3/M103867.html>

Funding: The work of the first and third authors was supported in part by NSF grants DMS-1115718 and DMS-1521009. The second author’s work was supported by the University of New Orleans through a Nick Müller Fellowship.

[†]Department of Mathematics, Southern University of Science and Technology of China, Shenzhen 518055, China, and Mathematics Department, Tulane University, New Orleans, LA 70118 (kurganov@math.tulane.edu).

[‡]Department of Mathematics, University of Innsbruck, A-6020 Innsbruck, Austria (martina.prugger@uibk.ac.at).

[§]Department of Mathematics, North Carolina State University, Raleigh, NC 27695 (twu18@ncsu.edu).

are also genuinely multidimensional upwind schemes, such as, e.g., the finite-volume evolution Galerkin methods (see [28, 29]), in which the flux integrals are approximated by using the multidimensional evolution operators. Compared to the standard upwind schemes, the interaction of complex multidimensional waves is typically captured by the finite-volume evolution Galerkin methods more accurately.

In this paper, we focus on Riemann-problem-solver-free Godunov-type central schemes, which were first introduced in [5] and [18] and then extended to higher orders [21, 26, 27, 30] and multiple space dimensions [1, 10, 22]. Central schemes use staggered grids in space and they are thus generically multidimensional. However, compared to upwind schemes they have larger numerical dissipation which often over-smears computed solutions, especially when the final computational time is large or when steady states are to be reached.

In order to reduce the numerical dissipation present in the staggered central schemes, a new class of central-upwind schemes was introduced in [13, 16, 17]. In the central-upwind schemes, the solution is first evolved (without solving any Riemann problems) in the control volumes whose sizes correspond to the local speeds of propagation and is then projected back onto the original grid (using a more accurate projection procedure, the numerical dissipation was further reduced in [12]). This way, one designs fully discrete central-upwind schemes, which are almost as accurate as upwind ones (they also admit a particularly simple semidiscrete form, which is obtained by taking the limit as the timestep goes to zero in the fully discrete scheme). However, only 1-D fully discrete schemes were derived in [12, 13, 16]. The derivation of the 2-D fully discrete central-upwind scheme is substantially more complicated, but as demonstrated in [12, 13, 14], one can construct genuinely multidimensional semidiscrete central-upwind schemes without explicitly writing their fully discrete originals.

In this paper, we rigorously derive a second-order fully discrete central-upwind scheme for general 2-D hyperbolic systems of conservation laws (1.1). To this end, we first reconstruct a piecewise linear approximant on the Cartesian grid, evolve it using the integral form of conservation laws to the next time level on a nonuniform quadrilateral grid (constructed with the help of one-sided local speeds of propagation), and then project it back onto the original Cartesian mesh. The new scheme is described in section 2. We then test the obtained fully discrete central-upwind scheme on a number of numerical examples and demonstrate its advantage compared with the semidiscrete central-upwind scheme from [12].

2. Two-dimensional fully discrete central-upwind scheme. We consider a uniform Cartesian mesh with the cells $C_{j,k} = [x_{j-\frac{1}{2}}, x_{j+\frac{1}{2}}] \times [y_{k-\frac{1}{2}}, y_{k+\frac{1}{2}}]$ centered at $x_j := (x_{j-\frac{1}{2}} + x_{j+\frac{1}{2}})/2$, $y_k := (y_{k-\frac{1}{2}} + y_{k+\frac{1}{2}})/2$ with $x_{j+\frac{1}{2}} - x_{j-\frac{1}{2}} \equiv \Delta x$, $y_{k+\frac{1}{2}} - y_{k-\frac{1}{2}} \equiv \Delta y$ for all j, k .

We assume that at a certain time level $t = t^n$ the computed cell averages of the solution,

$$\bar{U}_{j,k}^n \approx \frac{1}{\Delta x \Delta y} \iint_{C_{j,k}} U(x, y, t^n) dy dx,$$

are available. These cell averages are then evolved to the next time level $t = t^{n+1} := t^n + \Delta t^n$ in three consecutive steps: *reconstruction*, *evolution*, and *projection*, which will be described below in sections 2.1, 2.2, and 2.3, respectively.

2.1. Reconstruction. To construct a second-order scheme, we use a piecewise linear interpolant

$$(2.1) \quad \tilde{U}(x, y, t^n) = \sum_{j,k} \left[\bar{U}_{j,k}^n + (\mathbf{U}_x)_{j,k}^n(x - x_j) + (\mathbf{U}_y)_{j,k}^n(y - y_k) \right] \chi_{j,k}(x, y),$$

where $\chi_{j,k}(x, y)$ is the characteristic function of the interval $C_{j,k}$ and $(\mathbf{U}_x)_{j,k}^n$ and $(\mathbf{U}_y)_{j,k}^n$ stand for an (at least first-order) approximation of the x - and y -derivatives of \mathbf{U} at (x_j, y_k, t^n) . To avoid oscillations that may appear at the cell interfaces, a *nonlinear limiter* should be used in the evaluation of the slopes. We will use the generalized minmod limiter (see, e.g., [24, 30, 33, 35]):

$$(2.2) \quad \begin{aligned} (\mathbf{U}_x)_{j,k}^n &= \text{minmod} \left(\theta \Delta_x^+ \bar{U}_{j,k}^n, \Delta_x^0 \bar{U}_{j,k}^n, \theta \Delta_x^- \bar{U}_{j,k}^n \right), \\ (\mathbf{U}_y)_{j,k}^n &= \text{minmod} \left(\theta \Delta_y^+ \bar{U}_{j,k}^n, \Delta_y^0 \bar{U}_{j,k}^n, \theta \Delta_y^- \bar{U}_{j,k}^n \right), \end{aligned} \quad \theta \in [1, 2],$$

where Δ_x^\pm , Δ_x^0 , Δ_y^\pm , and Δ_y^0 are the standard divided difference operators:

$$\begin{aligned} \Delta_x^+(\cdot)_{j,k} &:= \frac{(\cdot)_{j+1,k} - (\cdot)_{j,k}}{\Delta x}, & \Delta_x^-(\cdot)_{j,k} &:= \frac{(\cdot)_{j,k} - (\cdot)_{j-1,k}}{\Delta x}, & \Delta_x^0(\cdot)_{j,k} &:= \frac{(\cdot)_{j+1,k} - (\cdot)_{j-1,k}}{2\Delta x}, \\ \Delta_y^+(\cdot)_{j,k} &:= \frac{(\cdot)_{j,k+1} - (\cdot)_{j,k}}{\Delta y}, & \Delta_y^-(\cdot)_{j,k} &:= \frac{(\cdot)_{j,k} - (\cdot)_{j,k-1}}{\Delta y}, & \Delta_y^0(\cdot)_{j,k} &:= \frac{(\cdot)_{j,k+1} - (\cdot)_{j,k-1}}{2\Delta y}, \end{aligned}$$

and the minmod function is defined as follows:

$$\text{minmod}(c_1, c_2, \dots, c_m) := \begin{cases} \min(c_1, c_2, \dots, c_m) & \text{if } c_i > 0 \ \forall i = 1, \dots, m, \\ \max(c_1, c_2, \dots, c_m) & \text{if } c_i < 0 \ \forall i = 1, \dots, m, \\ 0 & \text{otherwise.} \end{cases}$$

Note that larger values of θ correspond to sharper, more compressive, but also more oscillatory reconstructions (see, e.g., [24, 30]).

For the description of alternative nonlinear limiters that can be used instead of the minmod one in the reconstruction (2.1), we refer the reader to [20, 24, 30, 33, 35] and references therein.

Remark 2.1. We would like to emphasize that the minmod reconstruction (2.1), (2.2) as well as the reconstructions that will be described in the evolution (section 2.2) and projection (section 2.3) steps, is performed in a componentwise manner, that is, the minmod function in (2.2) is applied to each component of the vector \mathbf{U} directly without any characteristic decompositions.

2.2. Evolution. We first note that since we consider a hyperbolic problem, the discontinuities located across the cell interfaces upon completion of the reconstruction step will propagate at finite speeds. In the case of convex fluxes (see [15] and references therein for the discussion of the nonconvex cases), the one-sided local speeds at the midpoint of the cell edges can be estimated by

$$(2.3) \quad \begin{aligned} a_{j+\frac{1}{2},k}^+ &:= \max \left\{ \lambda_N \left(\frac{\partial \mathbf{F}}{\partial \mathbf{U}}(\mathbf{U}_{j+\frac{1}{2},k}^+) \right), \lambda_N \left(\frac{\partial \mathbf{F}}{\partial \mathbf{U}}(\mathbf{U}_{j+\frac{1}{2},k}^-) \right), 0 \right\}, \\ a_{j+\frac{1}{2},k}^- &:= \min \left\{ \lambda_1 \left(\frac{\partial \mathbf{F}}{\partial \mathbf{U}}(\mathbf{U}_{j+\frac{1}{2},k}^+) \right), \lambda_1 \left(\frac{\partial \mathbf{F}}{\partial \mathbf{U}}(\mathbf{U}_{j+\frac{1}{2},k}^-) \right), 0 \right\}, \\ b_{j,k+\frac{1}{2}}^+ &:= \max \left\{ \lambda_N \left(\frac{\partial \mathbf{G}}{\partial \mathbf{U}}(\mathbf{U}_{j,k+\frac{1}{2}}^+) \right), \lambda_N \left(\frac{\partial \mathbf{G}}{\partial \mathbf{U}}(\mathbf{U}_{j,k+\frac{1}{2}}^-) \right), 0 \right\}, \\ b_{j,k+\frac{1}{2}}^- &:= \min \left\{ \lambda_1 \left(\frac{\partial \mathbf{G}}{\partial \mathbf{U}}(\mathbf{U}_{j,k+\frac{1}{2}}^+) \right), \lambda_1 \left(\frac{\partial \mathbf{G}}{\partial \mathbf{U}}(\mathbf{U}_{j,k+\frac{1}{2}}^-) \right), 0 \right\}. \end{aligned}$$

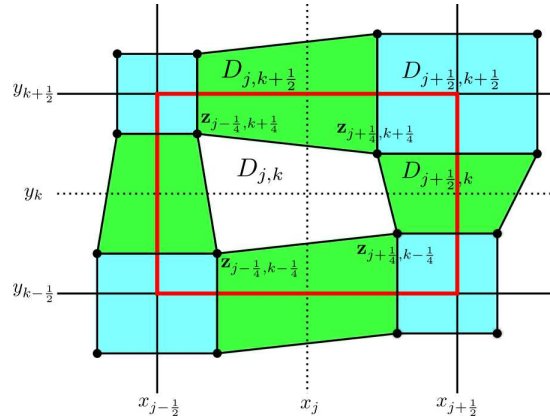


FIG. 1. Nonuniform control volumes in the 2-D set-up.

Here, $\lambda_1 < \lambda_2 < \dots < \lambda_N$ are the N eigenvalues of the corresponding Jacobians $\partial \mathbf{F} / \partial \mathbf{U}$ and $\partial \mathbf{G} / \partial \mathbf{U}$, and $\mathbf{U}_{j+\frac{1}{2},k}^\pm$ and $\mathbf{U}_{j,k+\frac{1}{2}}^\pm$ are the corresponding point values of the piecewise linear reconstruction (2.1):

$$\begin{aligned} \mathbf{U}_{j+\frac{1}{2},k}^- &:= \bar{\mathbf{U}}_{j,k}^n + \frac{\Delta x}{2} (\mathbf{U}_x)_{j,k}^n, & \mathbf{U}_{j+\frac{1}{2},k}^+ &:= \bar{\mathbf{U}}_{j+1,k}^n - \frac{\Delta x}{2} (\mathbf{U}_x)_{j+1,k}^n, \\ \mathbf{U}_{j,k+\frac{1}{2}}^- &:= \bar{\mathbf{U}}_{j,k}^n + \frac{\Delta y}{2} (\mathbf{U}_y)_{j,k}^n, & \mathbf{U}_{j,k+\frac{1}{2}}^+ &:= \bar{\mathbf{U}}_{j,k+1}^n - \frac{\Delta y}{2} (\mathbf{U}_y)_{j,k+1}^n. \end{aligned}$$

We refer the reader to [12, 17] for details.

Using the one-sided speed bounds (2.3), we split the computational domain $\bigcup_{j,k} C_{j,k}$ into the nonsymmetric subdomains $D_{j,k}$ (*central subdomains*), $D_{j+\frac{1}{2},k}$ and $D_{j,k+\frac{1}{2}}$ (*sides*), and $D_{j+\frac{1}{2},k+\frac{1}{2}}$ (*corners*) outlined in Figure 1. These subdomains are quadrilaterals with the vertices denoted by $\mathbf{z}_{j\pm\frac{1}{4},k\pm\frac{1}{4}} := (x_{j\pm\frac{1}{4},k\pm\frac{1}{4}}, y_{j\pm\frac{1}{4},k\pm\frac{1}{4}})$ with the following coordinates:

$$\begin{aligned} (2.4) \quad \mathbf{z}_{j+\frac{1}{4},k+\frac{1}{4}} &:= (x_{j+\frac{1}{2}} + \Delta t^n \min \{a_{j+\frac{1}{2},k}^-, a_{j+\frac{1}{2},k+1}^-\}, y_{k+\frac{1}{2}} + \Delta t^n \min \{b_{j,k+\frac{1}{2}}^-, b_{j+1,k+\frac{1}{2}}^-\}), \\ \mathbf{z}_{j-\frac{1}{4},k+\frac{1}{4}} &:= (x_{j-\frac{1}{2}} + \Delta t^n \max \{a_{j-\frac{1}{2},k}^+, a_{j-\frac{1}{2},k+1}^+\}, y_{k+\frac{1}{2}} + \Delta t^n \min \{b_{j,k+\frac{1}{2}}^-, b_{j-1,k+\frac{1}{2}}^-\}), \\ \mathbf{z}_{j-\frac{1}{4},k-\frac{1}{4}} &:= (x_{j-\frac{1}{2}} + \Delta t^n \max \{a_{j-\frac{1}{2},k}^+, a_{j-\frac{1}{2},k-1}^+\}, y_{k-\frac{1}{2}} + \Delta t^n \max \{b_{j,k-\frac{1}{2}}^+, b_{j-1,k-\frac{1}{2}}^+\}), \\ \mathbf{z}_{j+\frac{1}{4},k-\frac{1}{4}} &:= (x_{j+\frac{1}{2}} + \Delta t^n \min \{a_{j+\frac{1}{2},k}^-, a_{j+\frac{1}{2},k-1}^-\}, y_{k-\frac{1}{2}} + \Delta t^n \max \{b_{j,k-\frac{1}{2}}^+, b_{j+1,k-\frac{1}{2}}^+\}); \end{aligned}$$

see Figure 1. Notice that due to the finite speed of propagation, the evolved solution will remain smooth in the central subdomains $D_{j,k}$ and will be generically nonsmooth in the sides $D_{j+\frac{1}{2},k}$ and $D_{j,k+\frac{1}{2}}$ and corners $D_{j+\frac{1}{2},k+\frac{1}{2}}$ for all $t \in [t^n, t^{n+1})$. As one can see, the corners are rectangular, the sides are trapezoidal, while the central subdomains are general quadrilaterals.

Remark 2.2. Such a partition is possible only if our timestep is restricted by the following CFL-type condition:

$$(2.5) \quad \Delta t^n < \frac{1}{2} \cdot \min \left\{ \frac{\Delta x}{\max_{j,k} (a_{j+\frac{1}{2},k}^+, -a_{j+\frac{1}{2},k}^-)}, \frac{\Delta y}{\max_{j,k} (b_{j,k+\frac{1}{2}}^+, -b_{j,k+\frac{1}{2}}^-)} \right\}.$$

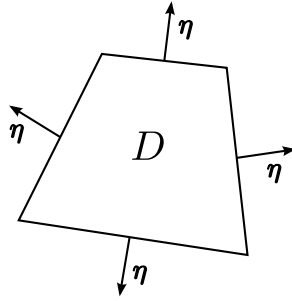


FIG. 2. General quadrilateral.

In order to avoid solving Riemann problems, the solution will be evolved in each of the aforementioned subdomains using the same technique as in [12, 13]. However, the 2-D set-up is now different from the ones in [12, 13], where the sides and corners were rectangular at the expense of the central subdomains, which had a complicated polygonal shape. This did not allow the authors in [12, 13] to express their 2-D fully discrete central-upwind scheme in closed form.

We now evolve the solution by integrating (1.1) over the central subdomains, sides, and corners in time from t^n to t^{n+1} . To this end, we consider a general quadrilateral D shown in Figure 2, for which we obtain the new cell averages over D (these cell averages are denoted as intermediate since they are yet to be projected onto the original grid as explained in section 2.3):

$$(2.6) \quad \bar{U}_D^{\text{int}} = \frac{1}{|D|} \iint_D \tilde{U}(x, y, t^n) dx dy - \frac{1}{|D|} \int_{t^n}^{t^{n+1}} \oint_{\partial D} [\eta^x \mathbf{F}(\mathbf{U}) + \eta^y \mathbf{G}(\mathbf{U})] ds dt,$$

where $\boldsymbol{\eta} = (\eta^x, \eta^y)^T$ is the outer unit normal vector to ∂D and the second term on the right-hand side (RHS) of (2.6) represents the fluxes across the four edges of the quadrilateral.

Next, we need to evaluate the integrals on the RHS of (2.6). The first term is obtained by integrating a piecewise linear polynomial over D . Depending on whether D is a central subdomain, side, or corner, one may need to split D into two or four parts according to the intersections of D with the boundaries of the original Cartesian cells, but in any case the evaluation of the first term on the RHS of (2.6) reduces to computing 2-D integrals of given linear functions over given quadrilaterals. We will denote the obtained cell averages of \tilde{U} over D at time $t = t^n$ by \bar{U}_D^n .

In order to present formulae for these cell averages, we first introduce the following notation. We split the original computational cell $C_{j,k}$ into the nine subdomains outlined in Figure 3: $D_{j,k}$ and

$$\begin{aligned} C_{j,k}^{\text{E}} &:= C_{j,k} \cap D_{j+\frac{1}{2},k}, & C_{j,k}^{\text{W}} &:= C_{j,k} \cap D_{j-\frac{1}{2},k}, & C_{j,k}^{\text{NE}} &:= C_{j,k} \cap D_{j+\frac{1}{2},k+\frac{1}{2}}, \\ C_{j,k}^{\text{NW}} &:= C_{j,k} \cap D_{j-\frac{1}{2},k+\frac{1}{2}}, & C_{j,k}^{\text{N}} &:= C_{j,k} \cap D_{j,k+\frac{1}{2}}, & C_{j,k}^{\text{S}} &:= C_{j,k} \cap D_{j,k-\frac{1}{2}}, \\ C_{j,k}^{\text{SE}} &:= C_{j,k} \cap D_{j+\frac{1}{2},k-\frac{1}{2}}, & C_{j,k}^{\text{SW}} &:= C_{j,k} \cap D_{j-\frac{1}{2},k-\frac{1}{2}}, \end{aligned}$$

and denote their centers of mass by $\mathbf{z}_{j,k}^{\text{C}}, \mathbf{z}_{j,k}^{\text{E}}, \mathbf{z}_{j,k}^{\text{W}}, \mathbf{z}_{j,k}^{\text{NE}}, \mathbf{z}_{j,k}^{\text{NW}}, \mathbf{z}_{j,k}^{\text{N}}, \mathbf{z}_{j,k}^{\text{S}}, \mathbf{z}_{j,k}^{\text{SE}},$ and $\mathbf{z}_{j,k}^{\text{SW}}$, respectively, where $\mathbf{z}_{j,k}^{\text{I}} := (x_{j,k}^{\text{I}}, y_{j,k}^{\text{I}})$, $\text{I} \in \{\text{E}, \text{W}, \text{N}, \text{S}, \text{NE}, \text{NW}, \text{SE}, \text{SW}\}$. The coordinates of the centers of mass can be easily computed and are provided in Appendix A.

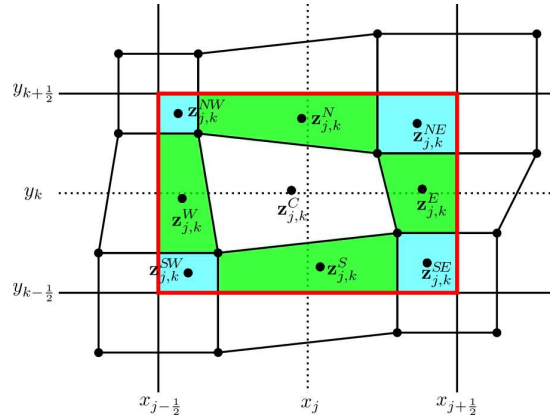


FIG. 3. Splitting of the original cell $C_{j,k}$ into nine subdomains and the centers of mass of each of the subdomains.

We then use the fact that in each of the subdomains $C_{j,k}^I$ the average value of \tilde{U} is simply equal to $\tilde{U}(z_{j,k}^I, t^n)$ and hence

$$\begin{aligned}
 (2.7) \quad \bar{U}_{D_{j,k}}^n &= \tilde{U}(z_{j,k}^C, t^n), \\
 \bar{U}_{D_{j+\frac{1}{2},k}}^n &= \frac{1}{|D_{j+\frac{1}{2},k}|} \left[|C_{j,k}^E| \tilde{U}(z_{j,k}^E, t^n) + |C_{j+1,k}^W| \tilde{U}(z_{j+1,k}^W, t^n) \right], \\
 \bar{U}_{D_{j,k+\frac{1}{2}}}^n &= \frac{1}{|D_{j,k+\frac{1}{2}}|} \left[|C_{j,k}^N| \tilde{U}(z_{j,k}^N, t^n) + |C_{j,k+1}^S| \tilde{U}(z_{j,k+1}^S, t^n) \right], \\
 \bar{U}_{D_{j+\frac{1}{2},k+\frac{1}{2}}}^n &= \frac{1}{|D_{j+\frac{1}{2},k+\frac{1}{2}}|} \left[|C_{j,k}^{NE}| \tilde{U}(z_{j,k}^{NE}, t^n) + |C_{j+1,k}^{NW}| \tilde{U}(z_{j+1,k}^{NW}, t^n) \right. \\
 &\quad \left. + |C_{j,k+1}^{SE}| \tilde{U}(z_{j,k+1}^{SE}, t^n) + |C_{j+1,k+1}^{SW}| \tilde{U}(z_{j+1,k+1}^{SW}, t^n) \right].
 \end{aligned}$$

Here, the areas $|C_{j,k}^E|$, $|C_{j,k}^E|$, $|C_{j,k}^E|$, $|C_{j,k}^E|$, $|C_{j,k}^E|$, $|C_{j,k}^E|$, and $|C_{j,k}^E|$ are given by (A.1), (A.2), and the areas of $D_{j+\frac{1}{2},k}$, $D_{j,k+\frac{1}{2}}$, and $D_{j+\frac{1}{2},k+\frac{1}{2}}$ are

$$\begin{aligned}
 (2.8) \quad |D_{j+\frac{1}{2},k}| &= |C_{j,k}^E| + |C_{j+1,k}^W|, \quad |D_{j,k+\frac{1}{2}}| = |C_{j,k}^N| + |C_{j,k+1}^S|, \\
 |D_{j+\frac{1}{2},k+\frac{1}{2}}| &= |C_{j,k}^{NE}| + |C_{j+1,k}^{NW}| + |C_{j,k+1}^{SE}| + |C_{j+1,k+1}^{SW}|.
 \end{aligned}$$

In order to evaluate the flux integrals on the RHS of (2.6), we need to split them into the sum of four integrals over the four edges of D . These integrals are then evaluated using the second-order trapezoidal (in space) and midpoint (in time) rules. We consider the following two possible cases.

Case 1. The nodes are $z_{\alpha,\beta-\frac{1}{4}}$ and $z_{\alpha,\beta+\frac{1}{4}}$, where $\alpha = j + \frac{1}{4}$ or $j - \frac{1}{4}$ and $\beta = k$ or $k + \frac{1}{2}$ for some j and k . Then, we define the numerical flux across the edge that connects these two nodes by

$$\begin{aligned}
 (2.9) \quad \mathbf{H}_{\alpha,\beta} &:= \frac{1}{\Delta t^n} \int_{t^n}^{t^{n+1}} \int_{z_{\alpha,\beta-\frac{1}{4}}}^{z_{\alpha,\beta+\frac{1}{4}}} \left[\eta_{\alpha,\beta}^x \mathbf{F}(\mathbf{U}) + \eta_{\alpha,\beta}^y \mathbf{G}(\mathbf{U}) \right] ds dt \\
 &\approx \frac{|z_{\alpha,\beta+\frac{1}{4}} - z_{\alpha,\beta-\frac{1}{4}}|}{2} \left\{ \eta_{\alpha,\beta}^x \left[\mathbf{F}(\mathbf{U}_{\alpha,\beta-\frac{1}{4}}^{n+\frac{1}{2}}) + \mathbf{F}(\mathbf{U}_{\alpha,\beta+\frac{1}{4}}^{n+\frac{1}{2}}) \right] \right. \\
 &\quad \left. + \eta_{\alpha,\beta}^y \left[\mathbf{G}(\mathbf{U}_{\alpha,\beta-\frac{1}{4}}^{n+\frac{1}{2}}) + \mathbf{G}(\mathbf{U}_{\alpha,\beta+\frac{1}{4}}^{n+\frac{1}{2}}) \right] \right\},
 \end{aligned}$$

where the unit normal vectors $\boldsymbol{\eta}_{\alpha,\beta}$ for $\beta = k$ and $\beta = k + \frac{1}{2}$ are

$$\boldsymbol{\eta}_{\alpha,k} = \frac{(y_{\alpha,k+\frac{1}{4}} - y_{\alpha,k-\frac{1}{4}}, x_{\alpha,k-\frac{1}{4}} - x_{\alpha,k+\frac{1}{4}})}{|z_{\alpha,\beta+\frac{1}{4}} - z_{\alpha,\beta-\frac{1}{4}}|} \quad \text{and} \quad \boldsymbol{\eta}_{\alpha,k+\frac{1}{2}} = (1, 0),$$

respectively.

Case 2. The nodes are $z_{\alpha-\frac{1}{4},\beta}$ and $z_{\alpha+\frac{1}{4},\beta}$, where $\alpha = j$ or $j + \frac{1}{2}$ and $\beta = k + \frac{1}{4}$ or $k - \frac{1}{4}$ for some j and k , and the numerical flux across the edge that connects these two nodes is

$$\begin{aligned}
 (2.10) \quad \mathbf{H}_{\alpha,\beta} &:= \frac{1}{\Delta t^n} \int_{t^n}^{t^{n+1}} \int_{z_{\alpha-\frac{1}{4},\beta}}^{z_{\alpha+\frac{1}{4},\beta}} \left[\eta_{\alpha,\beta}^x \mathbf{F}(\mathbf{U}) + \eta_{\alpha,\beta}^y \mathbf{G}(\mathbf{U}) \right] ds dt \\
 &\approx \frac{|z_{\alpha+\frac{1}{4},\beta} - z_{\alpha-\frac{1}{4},\beta}|}{2} \left\{ \eta_{\alpha,\beta}^x \left[\mathbf{F}(\mathbf{U}_{\alpha-\frac{1}{4},\beta}^{n+\frac{1}{2}}) + \mathbf{F}(\mathbf{U}_{\alpha+\frac{1}{4},\beta}^{n+\frac{1}{2}}) \right] \right. \\
 &\quad \left. + \eta_{\alpha,\beta}^y \left[\mathbf{G}(\mathbf{U}_{\alpha-\frac{1}{4},\beta}^{n+\frac{1}{2}}) + \mathbf{G}(\mathbf{U}_{\alpha+\frac{1}{4},\beta}^{n+\frac{1}{2}}) \right] \right\},
 \end{aligned}$$

where the unit normal vectors $\boldsymbol{\eta}_{\alpha,\beta}$ for $\alpha = j$ and $\alpha = j + \frac{1}{2}$ are

$$\boldsymbol{\eta}_{j,\beta} = \frac{(y_{j-\frac{1}{4},\beta} - y_{j+\frac{1}{4},\beta}, x_{j+\frac{1}{4},\beta} - x_{j-\frac{1}{4},\beta})}{|z_{\alpha+\frac{1}{4},\beta} - z_{\alpha-\frac{1}{4},\beta}|} \quad \text{and} \quad \boldsymbol{\eta}_{j+\frac{1}{2},\beta} = (0, 1),$$

respectively.

Since the solution at the points $z_{j\pm\frac{1}{4},k\pm\frac{1}{4}}$ is smooth for $t \in [t^n, t^{n+1})$, we obtain the midpoint values in (2.9) and (2.10) using the first two terms of the Taylor expansion in time, which results in the following second-order approximation:

$$\begin{aligned}
 (2.11) \quad \mathbf{U}_{j\pm\frac{1}{4},k\pm\frac{1}{4}}^{n+\frac{1}{2}} &\approx \mathbf{U}(z_{j\pm\frac{1}{4},k\pm\frac{1}{4}}, t^n) - \frac{\Delta t}{2} \left[\mathbf{F}(\mathbf{U}(z_{j\pm\frac{1}{4},k\pm\frac{1}{4}}, t^n))_x + \mathbf{G}(\mathbf{U}(z_{j\pm\frac{1}{4},k\pm\frac{1}{4}}, t^n))_y \right] \\
 &\approx \tilde{\mathbf{U}}(z_{j\pm\frac{1}{4},k\pm\frac{1}{4}}, t^n) - \frac{\Delta t}{2} \left[(\mathbf{F}(\mathbf{U}))_x^n_{j,k} + (\mathbf{G}(\mathbf{U}))_y^n_{j,k} \right],
 \end{aligned}$$

where the slopes $(\mathbf{F}(\mathbf{U}))_x^n_{j,k}$ and $(\mathbf{G}(\mathbf{U}))_y^n_{j,k}$ are obtained using the minmod limiter as follows:

$$\begin{aligned}
 (2.12) \quad (\mathbf{F}(\mathbf{U}))_x^n_{j,k} &= \text{minmod} \left(\theta \Delta_x^+ (\mathbf{F}(\bar{\mathbf{U}}_{j,k}^n)), \Delta_x^0 (\mathbf{F}(\bar{\mathbf{U}}_{j,k}^n)), \theta \Delta_x^- (\mathbf{F}(\bar{\mathbf{U}}_{j,k}^n)) \right), \\
 (\mathbf{G}(\mathbf{U}))_y^n_{j,k} &= \text{minmod} \left(\theta \Delta_y^+ (\mathbf{G}(\bar{\mathbf{U}}_{j,k}^n)), \Delta_y^0 (\mathbf{G}(\bar{\mathbf{U}}_{j,k}^n)), \theta \Delta_y^- (\mathbf{G}(\bar{\mathbf{U}}_{j,k}^n)) \right).
 \end{aligned}$$

Finally, equipped with the numerical fluxes (2.9)–(2.11), we obtain the following approximation of (2.6):

$$\bar{U}_{D_{\alpha,\beta}}^{\text{int}} = \bar{U}_{D_{\alpha,\beta}}^n - \frac{\Delta t^n}{|D_{\alpha,\beta}|} \left[\mathbf{H}_{\alpha+\frac{1}{4},\beta} - \mathbf{H}_{\alpha-\frac{1}{4},\beta} + \mathbf{H}_{\alpha,\beta+\frac{1}{4}} - \mathbf{H}_{\alpha,\beta-\frac{1}{4}} \right].$$

Remark 2.3. Note that if some of the one-sided local speeds $a_{j+\frac{1}{2},k}^\pm$ or $b_{j,k+\frac{1}{2}}^\pm$ are zero, then the corresponding quadrilaterals may degenerate to triangles. In order to avoid such a situation, one can replace (2.3) with

$$\begin{aligned} a_{j+\frac{1}{2},k}^+ &:= \max \left\{ \lambda_N \left(\frac{\partial \mathbf{F}}{\partial \mathbf{U}} (\mathbf{U}_{j+\frac{1}{2},k}^+) \right), \lambda_N \left(\frac{\partial \mathbf{F}}{\partial \mathbf{U}} (\mathbf{U}_{j+\frac{1}{2},k}^-) \right), \varepsilon \right\}, \\ a_{j+\frac{1}{2},k}^- &:= \min \left\{ \lambda_1 \left(\frac{\partial \mathbf{F}}{\partial \mathbf{U}} (\mathbf{U}_{j+\frac{1}{2},k}^+) \right), \lambda_1 \left(\frac{\partial \mathbf{F}}{\partial \mathbf{U}} (\mathbf{U}_{j+\frac{1}{2},k}^-) \right), -\varepsilon \right\}, \\ b_{j,k+\frac{1}{2}}^+ &:= \max \left\{ \lambda_N \left(\frac{\partial \mathbf{G}}{\partial \mathbf{U}} (\mathbf{U}_{j,k+\frac{1}{2}}^+) \right), \lambda_N \left(\frac{\partial \mathbf{G}}{\partial \mathbf{U}} (\mathbf{U}_{j,k+\frac{1}{2}}^-) \right), \varepsilon \right\}, \\ b_{j,k+\frac{1}{2}}^- &:= \min \left\{ \lambda_1 \left(\frac{\partial \mathbf{G}}{\partial \mathbf{U}} (\mathbf{U}_{j,k+\frac{1}{2}}^+) \right), \lambda_1 \left(\frac{\partial \mathbf{G}}{\partial \mathbf{U}} (\mathbf{U}_{j,k+\frac{1}{2}}^-) \right), -\varepsilon \right\}, \end{aligned}$$

where ε is a small positive number. In all of the numerical examples presented in section 3, we have taken $\varepsilon = 10^{-8}$.

Remark 2.4. We note that one can use the Taylor expansion similar to the one used in (2.11) to obtain the second-order accurate point values $\{\mathbf{U}_{j\pm\frac{1}{4},k\pm\frac{1}{4}}^{n+1}\}$ at the time level $t = t^{n+1}$:

$$\mathbf{U}_{j\pm\frac{1}{4},k\pm\frac{1}{4}}^{n+1} = \tilde{\mathbf{U}}(\mathbf{z}_{j\pm\frac{1}{4},k\pm\frac{1}{4}}, t^n) - \Delta t \left[(\mathbf{F}(\mathbf{U})_x)_{j,k}^n + (\mathbf{G}(\mathbf{U})_y)_{j,k}^n \right],$$

where the slopes $(\mathbf{F}(\mathbf{U})_x)_{j,k}^n$ and $(\mathbf{G}(\mathbf{U})_y)_{j,k}^n$ are, as before, given by (2.12). These point values will be used at the projection step, which will be presented in section 2.3.

2.3. Projection. At the final step, we project the intermediate solution, realized in terms of the cell averages $\{\bar{\mathbf{U}}_D^{\text{int}}\}$ and the point values $\{\mathbf{U}_{j\pm\frac{1}{4},k\pm\frac{1}{4}}^{n+1}\}$, onto the original uniform mesh. To this end, we use the evolved data to construct a conservative piecewise linear interpolant $\tilde{\mathbf{U}}^{\text{int}}(x, y)$, and then integrate it over the original cells $C_{j,k}$ to obtain the cell averages of \mathbf{U} at the new time level $t = t^{n+1}$:

$$(2.13) \quad \bar{\mathbf{U}}_{j,k}^{n+1} = \frac{1}{\Delta x \Delta y} \iint_{C_{j,k}} \tilde{\mathbf{U}}^{\text{int}}(x, y) \, dx \, dy.$$

We now provide a detailed description of the projection procedure. First, notice that since $D_{j,k} \subset C_{j,k}$ for all j, k , it is enough to take the constant pieces in the central subdomains, that is,

$$(2.14) \quad \tilde{\mathbf{U}}^{\text{int}}(x, y) = \bar{\mathbf{U}}_{D_{j,k}}^{\text{int}} \quad \text{for } (x, y) \in D_{j,k}.$$

We then consider the domain $D_{\alpha,\beta}$ with $(\alpha, \beta) = (j + \frac{1}{2}, k + \frac{1}{2}), (j, k + \frac{1}{2}),$ or $(j + \frac{1}{2}, k)$ outlined in Figure 4 (left). The interpolant $\tilde{\mathbf{U}}^{\text{int}}(x, y)$ there will consist of four linear pieces that continuously match along the segments connecting the point (x_α, y_β) with the vertices of $D_{\alpha,\beta}$; see Figure 4 (right). The values at the vertices are $\mathbf{U}_{\alpha\pm\frac{1}{4},\beta\pm\frac{1}{4}}^{n+1}$ and the value of $\tilde{\mathbf{U}}^{\text{int}}$ at (x_α, y_β) , which we define by $\mathbf{U}_{\alpha,\beta}^{n+1}$, is determined from the conservation requirement:

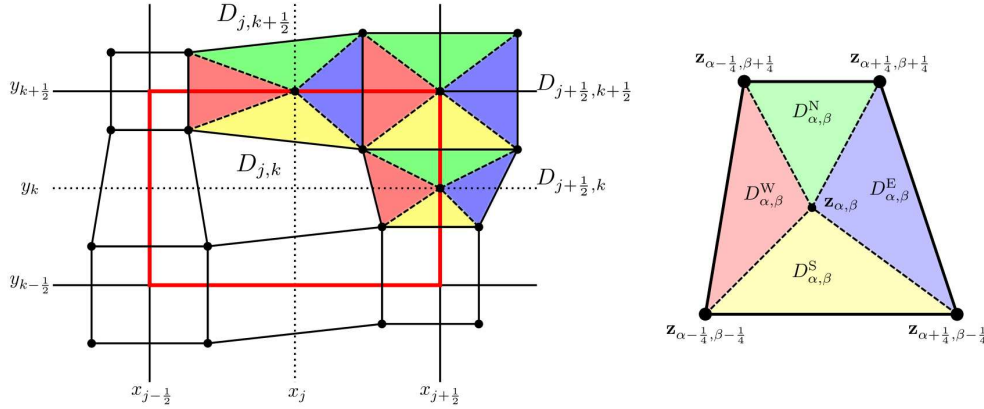


FIG. 4. Setting for the construction of $\tilde{U}^{\text{int}}(x, y)$ (left) and zoom at a sample subdomain $D_{\alpha, \beta}$, which is further split into the four smaller subdomains: $D_{\alpha, \beta}^{\text{N}}$, $D_{\alpha, \beta}^{\text{E}}$, $D_{\alpha, \beta}^{\text{S}}$, and $D_{\alpha, \beta}^{\text{W}}$ (right).

$$\frac{1}{|D_{\alpha, \beta}|} \iint_{D_{\alpha, \beta}} \tilde{U}^{\text{int}}(x, y) \, dx \, dy = \bar{U}_{D_{\alpha, \beta}}^{\text{int}},$$

which guarantees the second order of accuracy and results in

$$\begin{aligned} U_{\alpha, \beta}^{n+1} = & 3\bar{U}_{D_{\alpha, \beta}}^{\text{int}} - \frac{|D_{\alpha, \beta}^{\text{N}}| + |D_{\alpha, \beta}^{\text{E}}|}{|D_{\alpha, \beta}|} U_{\alpha + \frac{1}{4}, \beta + \frac{1}{4}}^{n+1} - \frac{|D_{\alpha, \beta}^{\text{E}}| + |D_{\alpha, \beta}^{\text{S}}|}{|D_{\alpha, \beta}|} U_{\alpha + \frac{1}{4}, \beta - \frac{1}{4}}^{n+1} \\ & - \frac{|D_{\alpha, \beta}^{\text{S}}| + |D_{\alpha, \beta}^{\text{W}}|}{|D_{\alpha, \beta}|} U_{\alpha - \frac{1}{4}, \beta - \frac{1}{4}}^{n+1} - \frac{|D_{\alpha, \beta}^{\text{W}}| + |D_{\alpha, \beta}^{\text{N}}|}{|D_{\alpha, \beta}|} U_{\alpha - \frac{1}{4}, \beta + \frac{1}{4}}^{n+1}. \end{aligned}$$

Here, the area $|D_{\alpha, \beta}|$ is given by (2.8) and the area of triangles $D_{\alpha, \beta}^{\text{N}}$, $D_{\alpha, \beta}^{\text{E}}$, $D_{\alpha, \beta}^{\text{S}}$, and $D_{\alpha, \beta}^{\text{W}}$ can be easily computed using the coordinates of their vertices.

We note that the constructed interpolant $\tilde{U}^{\text{int}}(x, y)$ may be oscillatory. In order to avoid appearance on new local extrema at (x_α, y_β) , we check whether

$$(2.15) \quad (U^{(i)})_{\alpha, \beta}^{n+1} > \max \left\{ \bar{U}_{D_{\alpha, \beta}}^{\text{int}}, \bar{U}_{D_{\alpha + \frac{1}{2}, \beta}}^{\text{int}}, \bar{U}_{D_{\alpha - \frac{1}{2}, \beta}}^{\text{int}}, \bar{U}_{D_{\alpha, \beta + \frac{1}{2}}}^{\text{int}}, \bar{U}_{D_{\alpha, \beta - \frac{1}{2}}}^{\text{int}} \right\}$$

or

$$(2.16) \quad (U^{(i)})_{\alpha, \beta}^{n+1} < \min \left\{ \bar{U}_{D_{\alpha, \beta}}^{\text{int}}, \bar{U}_{D_{\alpha + \frac{1}{2}, \beta}}^{\text{int}}, \bar{U}_{D_{\alpha - \frac{1}{2}, \beta}}^{\text{int}}, \bar{U}_{D_{\alpha, \beta + \frac{1}{2}}}^{\text{int}}, \bar{U}_{D_{\alpha, \beta - \frac{1}{2}}}^{\text{int}} \right\}$$

for some component i of U , and then replace the corresponding piecewise linear approximations with

$$(2.17) \quad (\tilde{U}^{(i)})^{\text{int}}(x, y) = (\bar{U}^{(i)})_{D_{\alpha, \beta}}^{\text{int}} \quad \text{for } (x, y) \in D_{\alpha, \beta}.$$

We note that the reconstruction correction procedure (2.15)–(2.17) locally reduces the order of the interpolant \tilde{U}^{int} to the first one, but this is the same clipping effect as in the case of the minmod limiter used at the reconstruction (see (2.2)) and evolution (see (2.13)) steps. We therefore expect that for smooth solutions the convergence rate will be two in the L^1 -norm and somewhat lower in the L^∞ -norm, as typically occurs when the minmod limiter is utilized.

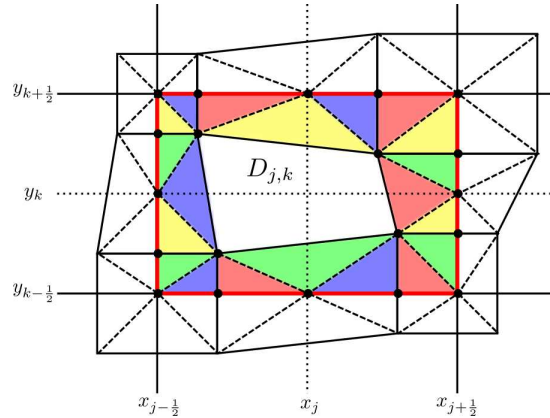


FIG. 5. Setting for the projection onto the original grid.

Finally, equipped with $\tilde{U}^{\text{int}}(x, y)$ we need to evaluate the integral on the RHS of (2.13), which is equal to the sum of $|D_{j,k}| \bar{U}_{D_{j,k}}^{\text{int}}$ and the areas of the triangles highlighted in Figure 5 multiplied by the values of \tilde{U}^{int} at their centers of mass. This can be easily done using the coordinates of the vertices of these triangles and the values of \tilde{U}^{int} there.

3. Numerical examples. In this section, we test the designed 2-D second-order fully discrete central-upwind scheme on a number of numerical examples. In Example 1, we test the accuracy of the scheme on the 2-D Burgers equation. In Examples 2–6, we apply the developed scheme to the Euler equations of gas dynamics

$$\begin{pmatrix} \rho \\ \rho u \\ \rho v \\ E \end{pmatrix}_t + \begin{pmatrix} \rho u \\ \rho u^2 + p \\ \rho uv \\ (E + p)u \end{pmatrix}_x + \begin{pmatrix} \rho v \\ \rho uv \\ \rho v^2 + p \\ (E + p)v \end{pmatrix}_y = 0.$$

Here, ρ is the density, u and v are x - and y -velocities, respectively, p is the pressure, and E is the total energy. The system is completed with the help of the equation of state, which for an ideal gas reads as

$$E = \frac{p}{\gamma - 1} + \frac{\rho(u^2 + v^2)}{2},$$

where γ is the specific heat ratio taken to be 1.4 in all of the reported numerical examples.

We use the minmod parameter $\theta = 1.3$ in (2.2) and the CFL number 0.475, which is slightly below the theoretical bound in (2.5). In Examples 3–6, we compare the results obtained by the designed second-order fully discrete central-upwind scheme with its semidiscrete counterpart from [12]. When the semidiscrete scheme is implemented, we use the same minmod parameter $\theta = 1.3$ and solve the time-dependent ODE systems (obtained after the semidiscretization) using the three-stage third-order strong stability preserving Runge–Kutta method; see, e.g., [7, 8].

TABLE 1
Example 1: Experimental convergence rates.

$\Delta x = \Delta y$	L^1 -error	Rate	L^∞ -error	Rate
1/40	1.52E-03	–	4.54E-03	–
1/80	4.10E-04	1.89	1.98E-03	1.20
1/160	9.92E-05	2.05	7.81E-04	1.34
1/320	2.36E-05	2.07	2.84E-04	1.46

We have also checked the efficiency of the proposed second-order fully discrete central-upwind scheme. Our numerical experiments clearly indicate that its computational cost is comparable with the cost of the second-order semidiscrete central-upwind scheme.

Example 1 (2-D Burgers equation—accuracy test). In the first example, we consider the 2-D Burgers equation,

$$u_t + \left(\frac{u^2}{2}\right)_x + \left(\frac{u^2}{2}\right)_y = 0,$$

subject to the periodic initial data given by

$$u(x, y, 0) = \frac{1}{4} + \frac{1}{2} \sin(2\pi(x + y)).$$

We use a square computational domain $[0, 1] \times [0, 1]$ with the periodic boundary condition and compute the solution until the small final time $t = 0.1$, at which the solution is still smooth. We use a sequence of uniform grids with $\Delta x = \Delta y = 1/40, 1/80, 1/160, \text{ and } 1/320$. We also compute the reference solution using a much finer mesh with $\Delta x = \Delta y = 1/1280$ and then measure the experimental convergence rates, reported in Table 1. As one can see, the second order of accuracy is achieved in the L^1 -norm, while the convergence rate measured in the L^∞ -norm is somewhat lower. The latter can be attributed to the fact that both the minmod limiter (used in the piecewise linear reconstruction (2.1), (2.2)) and a limited piecewise linear interpolation (used in the projection step described in section 2.3) lead to the order reduction near the local extrema of the computed solution.

Example 2 (Euler equations—accuracy test). In the second accuracy test, we consider the the Euler equations of gas dynamics subject to the periodic initial data:

$$\rho(x, y, 0) = 1 + \frac{1}{2} \sin(\pi(x + y)), \quad p(x, y, 0) = 1, \quad u(x, y, 0) = 1, \quad v(x, y, 0) = -0.7.$$

Note that the exact solution of this initial value problem can be easily obtained and it is given by $\rho(x, y, t) = 1 + \frac{1}{2} \sin(\pi(x + y - (u + v)t)), p(x, y, t) = 1, u(x, y, t) = 1, v(x, y, t) = -0.7$.

We use a square computational domain $[-1, 1] \times [-1, 1]$ with the periodic boundary condition and compute the solution until the final time $t = 0.1$ using uniform grids with $\Delta x = \Delta y = 1/50, 1/100, 1/200, \text{ and } 1/400$. In Table 2, we show the L^1 - and L^∞ -errors, which demonstrate that, as in Example 1, the experimental order of convergence of the proposed fully discrete scheme is about two in the L^1 -norm and between one and two in the L^∞ -norm.

TABLE 2
Example 2: Experimental convergence rates.

$\Delta x = \Delta y$	L^1 -error	Rate	L^∞ -error	Rate
1/50	1.06E-02	–	1.96E-03	–
1/100	2.45E-03	2.11	8.12E-04	1.27
1/200	5.76E-04	2.09	3.06E-04	1.41
1/400	1.25E-04	2.20	1.12E-04	1.46

Example 3 (steady vortex). In this example taken from [9], we consider the Euler equations of gas dynamics subject to the initial data corresponding to a steady vortex:

$$\begin{aligned} \rho(x, y, 0) &= \left(1 - \frac{\gamma - 1}{2} m_v^2 e^{1-x^2-y^2}\right)^{\frac{1}{\gamma-1}}, & u(x, y, 0) &= -m_v y e^{\frac{1-x^2-y^2}{2}}, \\ p(x, y, 0) &= \frac{1}{\gamma} \left(1 - \frac{\gamma - 1}{2} m_v^2 e^{1-x^2-y^2}\right)^{\frac{\gamma}{\gamma-1}}, & v(x, y, 0) &= m_v x e^{\frac{1-x^2-y^2}{2}}. \end{aligned}$$

Here, m_v is a strength of the vortex taken $m_v = 0.25$ as in [36].

We use the square computational domain $[-4, 4] \times [-4, 4]$, which is sufficiently large so that the effect of the vortex is negligibly small at the boundaries, and set zero-order extrapolation boundary conditions. The solution is evolved until the final time $t = 50$ using quite coarse uniform meshes with $\Delta x = \Delta y = 0.08$ and 0.04 . We note that both in [9] and [36], as well as in several other papers, this initial value problem was studied for the compressible Navier–Stokes equations rather than for the Euler ones. The presence of the viscous terms would be necessary for the experimental convergence study in this example.

Our goal is to compare the results obtained by the proposed fully discrete second-order central-upwind scheme with the ones computed by its semidiscrete counterpart. In Figure 6, we plot the cross section of the computed and exact densities along the line $y = x$. As one can clearly see, the solution computed by the fully discrete scheme is substantially more accurate, especially near the top part of the vortex.

Example 4 (2-D Riemann problem). We apply the designed scheme to a 2-D Riemann problem with the initial conditions prescribed with respect to the point

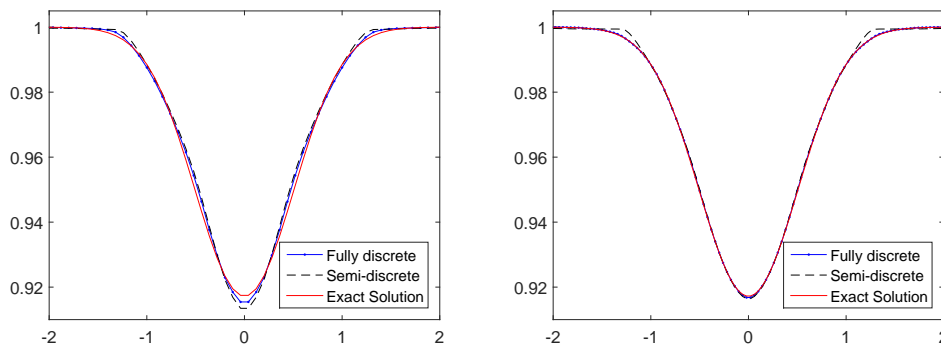


FIG. 6. *Example 3: Cross section of the density (ρ) computed by the second-order fully discrete and semidiscrete central-upwind schemes using uniform grids with $\Delta x = \Delta y = 0.08$ (left) and 0.04 (right). The exact solution is plotted using a solid line.*

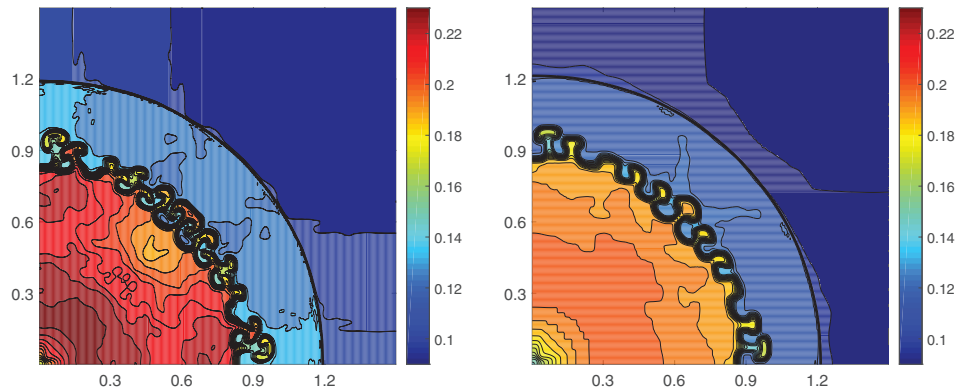


FIG. 8. *Example 5: Density (ρ) computed by the second-order fully discrete (left) and semidiscrete (right) central-upwind schemes.*

typically develops instabilities. Therefore, this example is a good test for the amount of numerical dissipation present in the studied schemes.

We use a uniform mesh with $\Delta x = \Delta y = 3/800$ and compute the solution until the final time $t = 3.2$ using both the fully discrete and semidiscrete second-order central-upwind schemes. The obtained results are shown in Figure 8. As one can clearly see, the contact surface computed by the fully discrete scheme is much “curlier” than the one obtained by the semidiscrete scheme: this demonstrates that the fully discrete scheme has substantially smaller amount of numerical dissipation.

Example 6 (implosion). In the final example, we consider the implosion problem from [25]. The initial conditions are

$$(\rho(x, y, 0), u(x, y, 0), v(x, y, 0), p(x, y, 0)) = \begin{cases} (0.125, 0, 0, 0.14), & |x| + |y| < 0.15, \\ (1.000, 0, 0, 1.00) & \text{otherwise.} \end{cases}$$

We use the square computation domain $[0, 0.3] \times [0, 0.3]$ and set the solid wall boundary conditions. As shown in [25], a jet of fluid is expected to emerge. However,

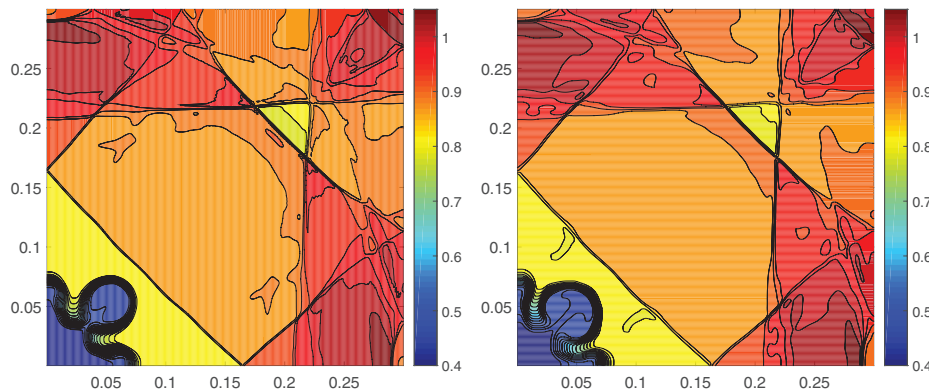


FIG. 9. *Example 6: Density (ρ) computed by the second-order fully discrete (left) and semidiscrete central-upwind schemes using $\Delta x = \Delta y = 3/4000$.*

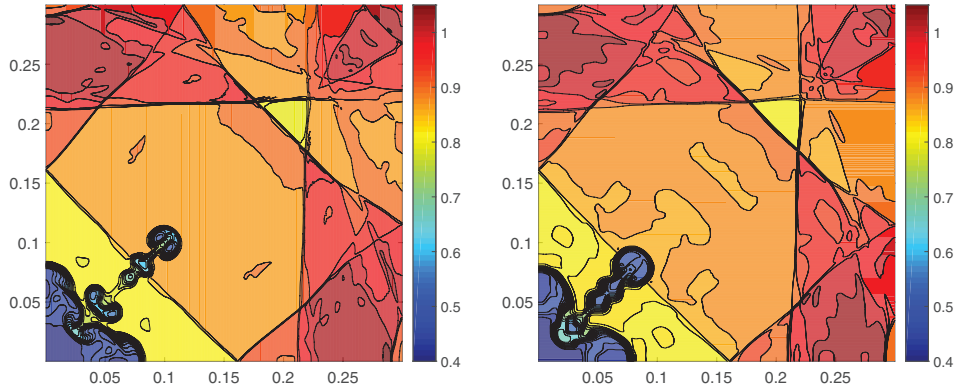


FIG. 10. Same as Figure 9, but with $\Delta x = \Delta y = 3/6000$.

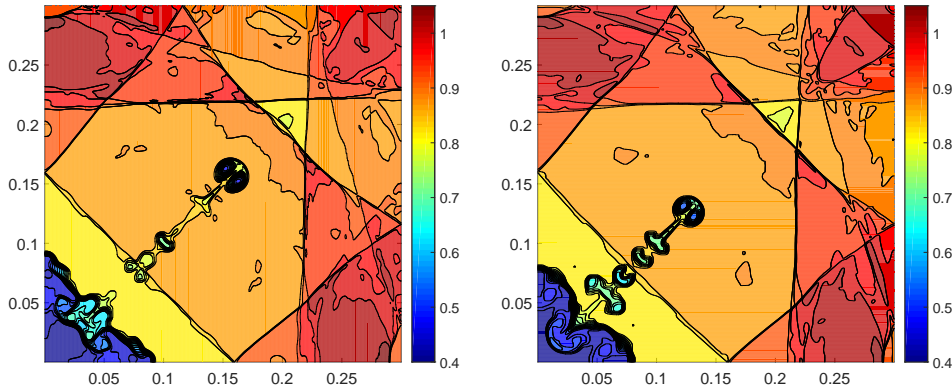


FIG. 11. Same as Figures 9 and 10, but with $\Delta x = \Delta y = 3/8000$.

the numerical dissipation present in many second-order schemes may smear the jet as demonstrated in [4, 25].

We compute the solution until the final time $t = 2.5$ using the second-order fully discrete and semidiscrete central-upwind schemes. We first use a uniform grid with $\Delta x = \Delta y = 3/4000$ and plot the obtained results in Figure 9. As one can see, though the results computed by the fully discrete scheme are a little sharper, no jet has been formed. We therefore increase the resolution by taking a finer uniform mesh with $\Delta x = \Delta y = 3/6000$ and show the obtained results in Figure 10, where one can observe the jets formed by both studied schemes. As one can see, however, the jet produced by the fully discrete scheme propagates faster, which indicates a lower amount of numerical diffusion present in the fully discrete scheme. This is confirmed by further mesh refinement; see Figure 11, where the results obtained using a uniform mesh with $\Delta x = \Delta y = 3/8000$ are shown.

4. Conclusions. In this paper, we have developed a new second-order fully discrete central-upwind scheme for 2-D hyperbolic systems of conservation laws. Equipped with the set of cell averages of the solution computed at a certain time moment, we have proceeded as follows: (i) reconstructed a piecewise linear interpolant

over the Cartesian mesh; (ii) used the one-sided local speeds of propagation at cell interfaces to construct a nonuniform quadrilateral mesh with the vertices located in the areas where the solution remains smooth until the next time level; (iii) evolved the solution realized in terms of the cell averages over this auxiliary quadrilateral mesh to the next time level; and (iv) projected the evolved solution onto the original Cartesian mesh using a sharp piecewise linear interpolant, which was designed to ensure both high resolution and nonoscillatory behavior of the resulting numerical solution.

The performance of the developed second-order fully discrete central-upwind scheme has been tested on a number of numerical examples for the 2-D Burgers equation and Euler equations of gas dynamics. We have first used the proposed scheme to compute smooth solutions, for which the second-order convergence rate has been achieved in the L^1 -norm and an advantage over the second-order semidiscrete central-upwind scheme has been demonstrated. In the last three examples, non smooth solutions of the Euler equations of gas dynamics were computed by both the fully discrete and semidiscrete central-upwind schemes, and we have demonstrated that the fully discrete scheme achieves sharper resolution of certain rough parts of the computed solutions, which suggests that the fully discrete scheme has a smaller amount of numerical dissipation than its semidiscrete counterpart.

The proposed second-order fully discrete central-upwind scheme can be extended to (unstructured) triangular meshes by evolving the solution over the auxiliary grid designed using the cell-vertex approach. We do not expect the triangular version of the scheme to be substantially more complicated than the Cartesian one. Extending the fully discrete central-upwind scheme to a higher than second order of accuracy seems to be a substantially more challenging but still accomplishable task. We plan to investigate both aforementioned extensions in our future work.

Appendix A. Coordinates of the centers of mass. In this section, we provide the coordinates of the centers of mass $z_{j,k}^C, z_{j,k}^E, z_{j,k}^W, z_{j,k}^{NE}, z_{j,k}^{NW}, z_{j,k}^N, z_{j,k}^S, z_{j,k}^{SE}$, and $z_{j,k}^{SW}$, outlined in Figure 3 and used in section 2.2 to project the reconstructed data onto the evolution cells $D_{j,k}, D_{j+\frac{1}{2},k}, D_{j,k+\frac{1}{2}},$ and $D_{j+\frac{1}{2},k+\frac{1}{2}}$.

First, the areas of the rectangles $C_{j,k}^{NE}, C_{j,k}^{NW}, C_{j,k}^{SE}$, and $C_{j,k}^{SW}$ are

$$\begin{aligned}
 |C_{j,k}^{NE}| &= (x_{j+\frac{1}{2}} - x_{j+\frac{1}{4},k+\frac{1}{4}})(y_{k+\frac{1}{2}} - y_{j+\frac{1}{4},k+\frac{1}{4}}), \\
 |C_{j,k}^{NW}| &= (x_{j-\frac{1}{4},k+\frac{1}{4}} - x_{j-\frac{1}{2}})(y_{k+\frac{1}{2}} - y_{j-\frac{1}{4},k+\frac{1}{4}}), \\
 |C_{j,k}^{SE}| &= (x_{j+\frac{1}{2}} - x_{j+\frac{1}{4},k-\frac{1}{4}})(y_{j+\frac{1}{4},k-\frac{1}{4}} - y_{k-\frac{1}{2}}), \\
 |C_{j,k}^{SW}| &= (x_{j-\frac{1}{4},k-\frac{1}{4}} - x_{j-\frac{1}{2}})(y_{j-\frac{1}{4},k-\frac{1}{4}} - y_{k-\frac{1}{2}}),
 \end{aligned}
 \tag{A.1}$$

and their centers of mass are

$$\begin{aligned}
 z_{j,k}^{NE} &= \left(\frac{x_{j+\frac{1}{4},k+\frac{1}{4}} + x_{j+\frac{1}{2}}}{2}, \frac{y_{j+\frac{1}{4},k+\frac{1}{4}} + y_{k+\frac{1}{2}}}{2} \right), \\
 z_{j,k}^{NW} &= \left(\frac{x_{j-\frac{1}{4},k+\frac{1}{4}} + x_{j-\frac{1}{2}}}{2}, \frac{y_{j-\frac{1}{4},k+\frac{1}{4}} + y_{k+\frac{1}{2}}}{2} \right), \\
 z_{j,k}^{SE} &= \left(\frac{x_{j+\frac{1}{4},k-\frac{1}{4}} + x_{j+\frac{1}{2}}}{2}, \frac{y_{j+\frac{1}{4},k-\frac{1}{4}} + y_{k-\frac{1}{2}}}{2} \right), \\
 z_{j,k}^{SW} &= \left(\frac{x_{j-\frac{1}{4},k-\frac{1}{4}} + x_{j-\frac{1}{2}}}{2}, \frac{y_{j-\frac{1}{4},k-\frac{1}{4}} + y_{k-\frac{1}{2}}}{2} \right).
 \end{aligned}$$

We then note that $C_{j,k}^E$, $C_{j,k}^W$, $C_{j,k}^N$, and $C_{j,k}^S$ are right-angled trapezoids with the areas

$$(A.2) \quad \begin{aligned} |C_{j,k}^E| &= \left(x_{j+\frac{1}{2}} - \frac{x_{j+\frac{1}{4},k+\frac{1}{4}} + x_{j+\frac{1}{4},k-\frac{1}{4}}}{2}\right)(y_{j+\frac{1}{4},k+\frac{1}{4}} - y_{j+\frac{1}{4},k-\frac{1}{4}}), \\ |C_{j,k}^W| &= \left(\frac{x_{j-\frac{1}{4},k+\frac{1}{4}} + x_{j-\frac{1}{4},k-\frac{1}{4}}}{2} - x_{j-\frac{1}{2}}\right)(y_{j-\frac{1}{4},k+\frac{1}{4}} - y_{j-\frac{1}{4},k-\frac{1}{4}}), \\ |C_{j,k}^N| &= \left(y_{k+\frac{1}{2}} - \frac{y_{j+\frac{1}{4},k+\frac{1}{4}} + y_{j-\frac{1}{4},k+\frac{1}{4}}}{2}\right)(x_{j+\frac{1}{4},k+\frac{1}{4}} - x_{j-\frac{1}{4},k+\frac{1}{4}}), \\ |C_{j,k}^S| &= \left(\frac{y_{j+\frac{1}{4},k-\frac{1}{4}} + y_{j-\frac{1}{4},k-\frac{1}{4}}}{2} - y_{k-\frac{1}{2}}\right)(x_{j+\frac{1}{4},k-\frac{1}{4}} - x_{j-\frac{1}{4},k-\frac{1}{4}}) \end{aligned}$$

and the centers of mass given by

$$\begin{aligned} z_{j,k}^E &= \left(\frac{x_{j+\frac{1}{4},k+\frac{1}{4}} + x_{j+\frac{1}{4},k-\frac{1}{4}} + x_{j+\frac{1}{2}}}{3} + \frac{(x_{j+\frac{1}{2}} - x_{j+\frac{1}{4},k+\frac{1}{4}})(x_{j+\frac{1}{2}} - x_{j+\frac{1}{4},k-\frac{1}{4}})}{3(2x_{j+\frac{1}{2}} - x_{j+\frac{1}{4},k+\frac{1}{4}} - x_{j+\frac{1}{4},k-\frac{1}{4}})}\right. \\ &\quad \left. \frac{y_{j+\frac{1}{4},k+\frac{1}{4}} + y_{j+\frac{1}{4},k-\frac{1}{4}}}{2} - \frac{(y_{j+\frac{1}{4},k+\frac{1}{4}} - y_{j+\frac{1}{4},k-\frac{1}{4}})(x_{j+\frac{1}{4},k+\frac{1}{4}} - x_{j+\frac{1}{4},k-\frac{1}{4}})}{6(2x_{j+\frac{1}{2}} - x_{j+\frac{1}{4},k+\frac{1}{4}} - x_{j+\frac{1}{4},k-\frac{1}{4}})}\right), \\ z_{j,k}^W &= \left(\frac{x_{j-\frac{1}{4},k+\frac{1}{4}} + x_{j-\frac{1}{4},k-\frac{1}{4}} + x_{j-\frac{1}{2}}}{3} - \frac{(x_{j-\frac{1}{4},k+\frac{1}{4}} - x_{j-\frac{1}{2}})(x_{j-\frac{1}{4},k-\frac{1}{4}} - x_{j-\frac{1}{2}})}{3(x_{j-\frac{1}{4},k+\frac{1}{4}} + x_{j-\frac{1}{4},k-\frac{1}{4}} - 2x_{j-\frac{1}{2}})}\right. \\ &\quad \left. \frac{y_{j-\frac{1}{4},k+\frac{1}{4}} + y_{j-\frac{1}{4},k-\frac{1}{4}}}{2} + \frac{(y_{j-\frac{1}{4},k+\frac{1}{4}} - y_{j-\frac{1}{4},k-\frac{1}{4}})(x_{j-\frac{1}{4},k+\frac{1}{4}} - x_{j-\frac{1}{4},k-\frac{1}{4}})}{6(x_{j-\frac{1}{4},k+\frac{1}{4}} + x_{j-\frac{1}{4},k-\frac{1}{4}} - 2x_{j-\frac{1}{2}})}\right), \\ z_{j,k}^N &= \left(\frac{x_{j-\frac{1}{4},k+\frac{1}{4}} + x_{j+\frac{1}{4},k+\frac{1}{4}}}{2} - \frac{(x_{j+\frac{1}{4},k+\frac{1}{4}} - x_{j-\frac{1}{4},k+\frac{1}{4}})(y_{j+\frac{1}{4},k+\frac{1}{4}} - y_{j-\frac{1}{4},k+\frac{1}{4}})}{6(2y_{k+\frac{1}{2}} - y_{j+\frac{1}{4},k+\frac{1}{4}} - y_{j-\frac{1}{4},k+\frac{1}{4}})}\right. \\ &\quad \left. \frac{y_{j-\frac{1}{4},k+\frac{1}{4}} + y_{j+\frac{1}{4},k+\frac{1}{4}} + y_{k+\frac{1}{2}}}{3} + \frac{(y_{k+\frac{1}{2}} - y_{j+\frac{1}{4},k+\frac{1}{4}})(y_{k+\frac{1}{2}} - y_{j-\frac{1}{4},k+\frac{1}{4}})}{3(2y_{k+\frac{1}{2}} - y_{j+\frac{1}{4},k+\frac{1}{4}} - y_{j-\frac{1}{4},k+\frac{1}{4}})}\right), \\ z_{j,k}^S &= \left(\frac{x_{j-\frac{1}{4},k-\frac{1}{4}} + x_{j+\frac{1}{4},k-\frac{1}{4}}}{2} + \frac{(x_{j+\frac{1}{4},k-\frac{1}{4}} - x_{j-\frac{1}{4},k-\frac{1}{4}})(y_{j+\frac{1}{4},k-\frac{1}{4}} - y_{j-\frac{1}{4},k-\frac{1}{4}})}{6(y_{j+\frac{1}{4},k-\frac{1}{4}} + y_{j-\frac{1}{4},k-\frac{1}{4}} - 2y_{k-\frac{1}{2}})}\right. \\ &\quad \left. \frac{y_{j-\frac{1}{4},k-\frac{1}{4}} + y_{j+\frac{1}{4},k-\frac{1}{4}} + y_{k-\frac{1}{2}}}{3} - \frac{(y_{j+\frac{1}{4},k-\frac{1}{4}} - y_{k-\frac{1}{2}})(y_{j-\frac{1}{4},k-\frac{1}{4}} - y_{k-\frac{1}{2}})}{3(y_{j+\frac{1}{4},k-\frac{1}{4}} + y_{j-\frac{1}{4},k-\frac{1}{4}} - 2y_{k-\frac{1}{2}})}\right). \end{aligned}$$

Finally, the coordinates of $z_{j,k}^C$ are computed using the fact that the center of mass of the cell $C_{j,k}$ is (x_j, y_k) , which leads to

$$z_{j,k}^C = \frac{1}{|D_{j,k}|} \left[|C_{j,k}|(x_j, y_k) - |C_{j,k}^E|z_{j,k}^E - |C_{j,k}^W|z_{j,k}^W - |C_{j,k}^N|z_{j,k}^N - |C_{j,k}^S|z_{j,k}^S \right. \\ \left. - |C_{j,k}^{NE}|z_{j,k}^{NE} - |C_{j,k}^{NW}|z_{j,k}^{NW} - |C_{j,k}^{SE}|z_{j,k}^{SE} - |C_{j,k}^{SW}|z_{j,k}^{SW} \right],$$

where $|C_{j,k}^{NE}|$, $|C_{j,k}^{NW}|$, $|C_{j,k}^{SE}|$, and $|C_{j,k}^{SW}|$ are given by (A.1), $|C_{j,k}^E|$, $|C_{j,k}^W|$, $|C_{j,k}^N|$, and $|C_{j,k}^S|$ are given by (A.2), and

$$(A.3) \quad |D_{j,k}| = |C_{j,k}| - |C_{j,k}^E| - |C_{j,k}^W| - |C_{j,k}^N| - |C_{j,k}^S| - |C_{j,k}^{NE}| - |C_{j,k}^{NW}| - |C_{j,k}^{SE}| - |C_{j,k}^{SW}|.$$

Acknowledgment. A part of this research was conducted during the 2013–2014 academic year, when the second author visited the University of New Orleans.

REFERENCES

- [1] P. ARMINJON, M.-C. VIALON, AND A. MADRANE, *A finite volume extension of the Lax-Friedrichs and Nessyahu-Tadmor schemes for conservation laws on unstructured grids*, Int. J. Comput. Fluid Dyn., 9 (1997), pp. 1–22.
- [2] M. BEN-ARTZI AND J. FALCOVITZ, *Generalized Riemann Problems in Computational Fluid Dynamics*, Cambridge Monogr. Appl. Comput. Math. 11, Cambridge University Press, Cambridge, UK, 2003.
- [3] S. BENZONI-GAVAGE AND D. SERRE, *Multidimensional Hyperbolic Partial Differential Equations: First-Order Systems and Applications*, Oxford Math. Monogr., Oxford University Press, New York, 2007.
- [4] J. DEWAR, A. KURGANOV, AND M. LEOPOLD, *Pressure-based adaption indicator for compressible Euler equations*, Numer. Methods Partial Differential Equations, 31 (2015), pp. 1844–1874.
- [5] K. O. FRIEDRICHS, *Symmetric hyperbolic linear differential equations*, Comm. Pure Appl. Math., 7 (1954), pp. 345–392.
- [6] E. GODLEWSKI AND P.-A. RAVIART, *Numerical Approximation of Hyperbolic Systems of Conservation Laws*, Appl. Math. Sci. 118, Springer-Verlag, New York, 1996.
- [7] S. GOTTLIEB, D. KETCHESON, AND C.-W. SHU, *Strong Stability Preserving Runge-Kutta and Multistep Time Discretizations*, World Scientific, Hackensack, NJ, 2011.
- [8] S. GOTTLIEB, C.-W. SHU, AND E. TADMOR, *Strong stability-preserving high-order time discretization methods*, SIAM Rev., 43 (2001), pp. 89–112.
- [9] O. INOUE AND Y. HATTORI, *Sound generation by shock-vortex interactions*, J. Fluid Mech., 380 (1999), pp. 81–116.
- [10] G.-S. JIANG AND E. TADMOR, *Nonoscillatory central schemes for multidimensional hyperbolic conservation laws*, SIAM J. Sci. Comput., 19 (1998), pp. 1892–1917.
- [11] D. KRÖNER, *Numerical Schemes for Conservation Laws*, Wiley-Teubner Ser. Adv. Numer. Math., Wiley, Chichester, UK, 1997.
- [12] A. KURGANOV AND C.-T. LIN, *On the reduction of numerical dissipation in central-upwind schemes*, Commun. Comput. Phys., 2 (2007), pp. 141–163.
- [13] A. KURGANOV, S. NOELLE, AND G. PETROVA, *Semi-discrete central-upwind scheme for hyperbolic conservation laws and Hamilton-Jacobi equations*, SIAM J. Sci. Comput., 23 (2001), pp. 707–740.
- [14] A. KURGANOV AND G. PETROVA, *A third-order semi-discrete genuinely multidimensional central scheme for hyperbolic conservation laws and related problems*, Numer. Math., 88 (2001), pp. 683–729.
- [15] A. KURGANOV, G. PETROVA, AND B. POPOV, *Adaptive semi-discrete central-upwind schemes for nonconvex hyperbolic conservation laws*, SIAM J. Sci. Comput., 29 (2007), pp. 2381–2401.
- [16] A. KURGANOV AND E. TADMOR, *New high resolution central schemes for nonlinear conservation laws and convection-diffusion equations*, J. Comput. Phys., 160 (2000), pp. 241–282.
- [17] A. KURGANOV AND E. TADMOR, *Solution of two-dimensional Riemann problems for gas dynamics without Riemann problem solvers*, Numer. Methods Partial Differential Equations, 18 (2002), pp. 584–608.
- [18] P. D. LAX, *Weak solutions of nonlinear hyperbolic equations and their numerical computation*, Comm. Pure Appl. Math., 7 (1954), pp. 159–193.
- [19] P. D. LAX AND X.-D. LIU, *Solution of two-dimensional Riemann problems of gas dynamics by positive schemes*, SIAM J. Sci. Comput., 19 (1998), pp. 319–340 (electronic).
- [20] R. J. LEVEQUE, *Finite Volume Methods for Hyperbolic Problems*, Cambridge Texts Appl. Math., Cambridge University Press, Cambridge, UK, 2002.
- [21] D. LEVY, G. PUPPO, AND G. RUSSO, *Central WENO schemes for hyperbolic systems of conservation laws*, M2AN Math. Model. Numer. Anal., 33 (1999), pp. 547–571.
- [22] D. LEVY, G. PUPPO, AND G. RUSSO, *A fourth-order central WENO scheme for multidimensional hyperbolic systems of conservation laws*, SIAM J. Sci. Comput., 24 (2002), pp. 480–506.
- [23] J. LI, T. ZHANG, AND S. YANG, *The Two-Dimensional Riemann Problem in Gas Dynamics*, Pitman Monogr. Surveys Pure Appl. Math. 98, Longman, Harlow, UK, 1998.
- [24] K.-A. LIE AND S. NOELLE, *On the artificial compression method for second-order nonoscillatory central difference schemes for systems of conservation laws*, SIAM J. Sci. Comput., 24 (2003), pp. 1157–1174.
- [25] R. LISKA AND B. WENDROFF, *Comparison of several difference schemes on 1D and 2D test problems for the Euler equations*, SIAM J. Sci. Comput., 25 (2003), pp. 995–1017.

- [26] X.-D. LIU AND S. OSHER, *Nonoscillatory high order accurate self-similar maximum principle satisfying shock capturing schemes. I*, SIAM J. Numer. Anal., 33 (1996), pp. 760–779.
- [27] X.-D. LIU AND E. TADMOR, *Third order nonoscillatory central scheme for hyperbolic conservation laws*, Numer. Math., 79 (1998), pp. 397–425.
- [28] M. LUKÁČOVÁ-MEDVIĐOVÁ, K. W. MORTON, AND G. WARNECKE, *Evolution Galerkin methods for hyperbolic systems in two space dimensions*, Math. Comp., 69 (2000), pp. 1355–1384.
- [29] M. LUKÁČOVÁ-MEDVIĐOVÁ, K. W. MORTON, AND G. WARNECKE, *Finite volume evolution Galerkin methods for hyperbolic systems*, SIAM J. Sci. Comput., 26(1) (2004), pp. 1–30.
- [30] H. NESSYAHU AND E. TADMOR, *Nonoscillatory central differencing for hyperbolic conservation laws*, J. Comput. Phys., 87 (1990), pp. 408–463.
- [31] C. W. SCHULZ-RINNE, *Classification of the Riemann problem for two-dimensional gas dynamics*, SIAM J. Math. Anal., 24 (1993), pp. 76–88.
- [32] C. W. SCHULZ-RINNE, J. P. COLLINS, AND H. M. GLAZ, *Numerical solution of the Riemann problem for two-dimensional gas dynamics*, SIAM J. Sci. Comput., 14 (1993), pp. 1394–1394.
- [33] P. K. SWEBY, *High resolution schemes using flux limiters for hyperbolic conservation laws*, SIAM J. Numer. Anal., 21 (1984), pp. 995–1011.
- [34] E. F. TORO, *Riemann Solvers and Numerical Methods for Fluid Dynamics: A Practical Introduction*, 3rd ed., Springer-Verlag, Berlin, 2009.
- [35] B. VAN LEER, *Towards the ultimate conservative difference scheme. V. A second-order sequel to Godunov’s method*, J. Comput. Phys., 32 (1979), pp. 101–136.
- [36] S. ZHANG, Y.-T. ZHANG, AND C.-W. SHU, *Multistage interaction of a shock wave and a strong vortex*, Phys. Fluids, 17 (2005), 116101.
- [37] T. ZHANG AND Y. ZHENG, *Conjecture on the structure of solutions of the Riemann problem for two-dimensional gas dynamics systems*, SIAM J. Math. Anal., 21 (1990), pp. 593–630.
- [38] Y. ZHENG, *Systems of Conservation Laws: Two-Dimensional Riemann Problems*, Progr. Non-linear Differential Equations Appl. 38, Birkhäuser Boston, Boston, MA, 2001.